Multiscale modelling of matrix-crack percolation and gas leakage in fibre-reinforced composites

Wenkai Chang[1], Francis Rose[1], Garth Pearce[1], Luke Djukic[1,2], Anthony Kinloch[3], Chun-Hui Wang[1*]

[1] School of Mechanical and Manufacturing Engineering, University of New South Wales, Sydney, Australia
[2] Omni Tanker Pty Ltd, Smeaton Grange, NSW, Australia
[3] Department of Mechanical Engineering, Imperial, South Kensington Campus, London SW7 2AZ, UK.

Abstract

A multiscale framework is presented for predicting matrix-crack percolation and gas leakage in fibre-reinforced composites without empirical calibration. By eliminating fitting parameters, the approach provides clear advantages over existing models. A new continuum formulation enriched by a micromechanical damage model is first developed to predict matrix-crack spacing in individual plies, overcoming the dependence of conventional methods on destructive experimental measurements. By explicitly analysing fibres, matrix, and fibre-matrix interfaces, the formulation significantly reduces input requirements to a small set of constituent properties obtainable through standardized testing. The outputs are subsequently upscaled into a laminate-level continuum damage mechanics model to determine matrix-crack spacing as a function of applied strain. This crack-spacing information defines the geometry of a representative unit-cell model used to quantify throat areas at crack intersections. Unlike previous approaches that assume arbitrary delamination lengths, the present framework provides a physically based determination of throat areas. These micro-meso scale predictions are then coupled with an orifice flow model to enable complete leak-rate prediction of macroscale structures without empirical inputs. This novel multiscale framework is shown to accurately reproduce experimental leakage data. Its capability for design and certification of cryogenic fuel storage vessels is demonstrated by quantifying the benefit of increased matrix toughness in enhancing resistance to gas leakage.

Keywords: Multiscale Modelling; Matrix Crack; Digital Twin; Carbon Fibre Composites; Pressure Vessels; Leak rate.

* Corresponding author: chun.h.wang@unsw.edu.au (C.H. Wang).

1. Introduction

Predicting the leakage-threshold condition, i.e. the pressure at which carbon fibre reinforced polymer (CFRP) vessels begin to exceed allowable gas leak rates, remains a major challenge for all-composite vessel design and certification [1]. Under multiaxial loading conditions, matrix-dominated damage evolves from dispersed microcracks to matrix cracks (i.e. transverse cracks that extend through the layer thickness and span the laminate width, viz., cracks that split plies [2]) and eventually to multilayer intersecting cracks, denoted as

percolation, that provide connected through-thickness pathways for gas leakage [3-6] (see Fig. 1). This percolation threshold is typically marked by an abrupt increase in leak rate that is several orders of magnitude higher than that due to diffusion through pristine laminates, or laminates containing only isolated matrix cracks (typically $< 10^{-10}$ $m^3/m^2/s$, as measured for He and H_2 at room temperature [7-9]). Existing qualification standards and design guidelines for CFRP hydrogen vessels [10-17] adopt a leak-before-burst (LBB) safety philosophy to prevent catastrophic rupture while enforcing explicit allowable leak-rate limits. For example, an H_2 allowable leak rate of 5.74×10^{-6} $m^3/m^2/s$ is prescribed as the limit for cryogenic launch-vehicle hydrogen tanks [17], and substantially more stringent limits apply for on-road hydrogen vehicle in international standards [10-12]. While clear pass-or-fail certification criteria have thus been defined at a prescribed limit pressure [10-12, 15, 16], there remains a lack of mechanics-based tools for predicting the leakage-threshold load or pressure at which limit-exceeding leakage occurs. Consequently, the current design practice for all-composite pressure vessels remains *ad hoc* and reliant on costly trial-and-error physical prototyping and full-scale testing with high development cost and time-to-qualification.

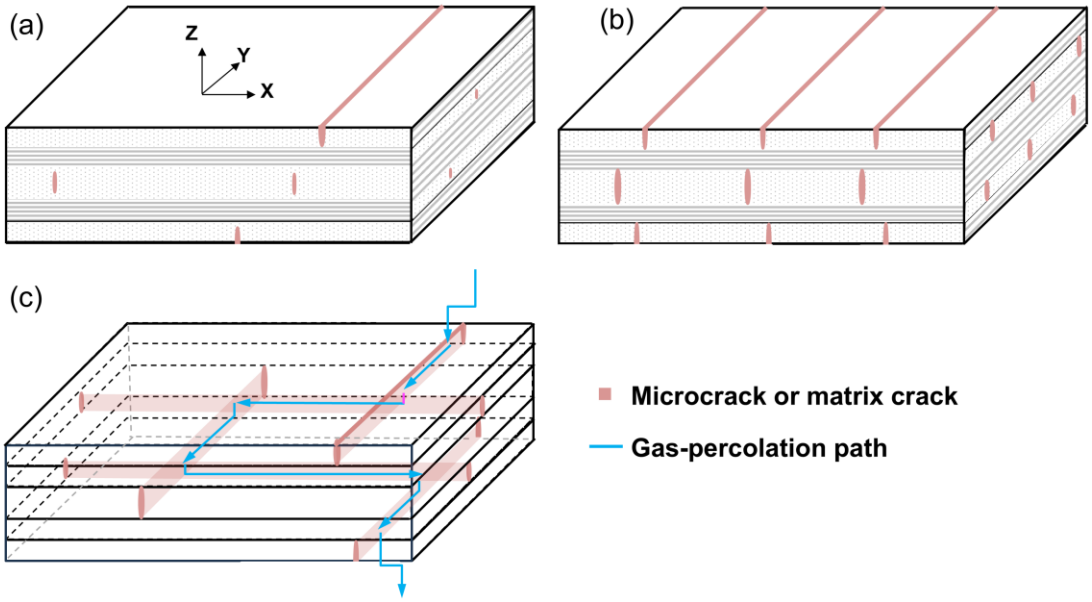

Fig. 1 Matrix-dominated damage progression in a cross-ply CFRP laminate under biaxial tension and its implication for leakage-controlled qualification. (a) Through-thickness growth of dispersed microcracks leading to matrix cracks that split plies. (b) Multiplication of matrix cracks with increasing load, forming a quasi-periodic crack array. (c) Linking of multilayer intersecting matrix cracks forms a through-thickness crack network causing gas-percolation leakage.

Pioneering studies by Kumazawa and co-workers [7, 18, 19] established systematic biaxial-tension experiments and a semi-analytical framework linking matrix-dominated damage in CFRP laminates to through-thickness gas leakage. In these analyses, leakage is modelled as a network-flow problem in which gas transport across the laminate is governed by the local conductance at intersections between matrix cracks in adjacent

plies, commonly idealized as orifice-type throats within a multilayer conductance model [7, 20], as shown in Fig. 2(a). Previous work identified two key parameters for leakage prediction [7, 18-21]: (a) the ply-wise matrix crack density (ρ) and (b) the crack-tip opening displacements (CTODs or Δ) at the intersection as depicted in Fig. 2(b), which characterizes the total throat area (A), with the intersection conductance being assumed to be proportional to A through an empirically determined constant.

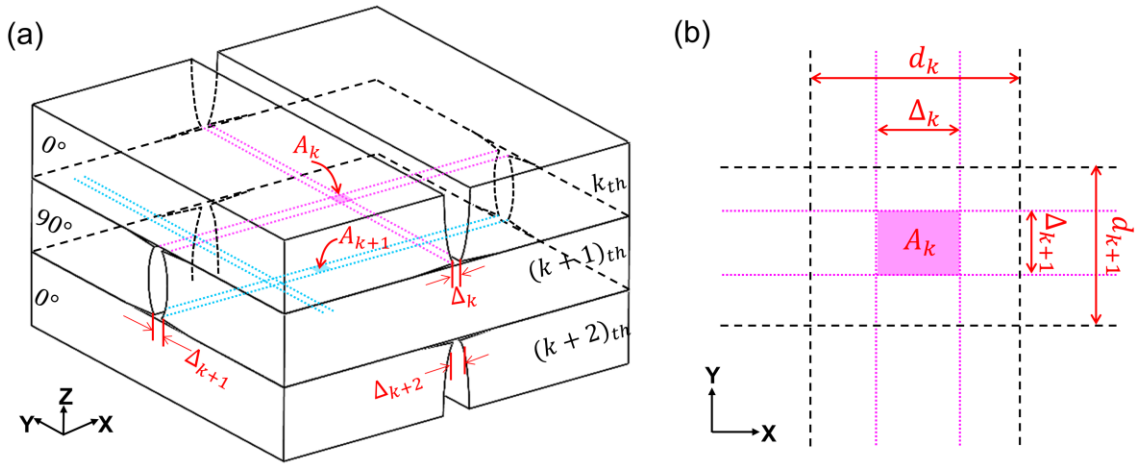

Fig. 2 Schematic of the multilayer conductance leakage model for cross-ply CFRP laminates. (a) Intersections between matrix cracks in adjacent plies form crack-intersection throats at ply interfaces. (b) Plan-view definition of an intersection throat at the k-th interface: the effective opening is characterized by the CTODs Δ_k and Δ_{k+1}, with finite opening enabled by the associated delamination with lengths d_k and d_{k+1}; the resulting throat area A_k governs the local intersection conductance.

Subsequent work by Kumazawa and Whitcomb [22] employed a combination of finite-element analysis (FEA) and computational fluid dynamics (CFD) to predict leak rates. The FEA used a unit cell with periodic boundary conditions to model a doubly-periodic array of matrix cracks, but the appropriate crack spacings corresponding to the varying applied load levels was obtained from the experimental measurements reported in [7]. This unit cell also featured delaminations of various prescribed lengths at the inter-ply interfaces, with the appropriate delamination length being determined by trial and error to ensure that predicted leak rates under thermal loading only, without mechanical load, matched the experimental values in [7]. The same fitted delamination length was then employed for predicting leak rates under mechanical load. The model for CFD calculations prescribed simple analytical shapes for the crack opening displacements (linear in outer plies and quadratic for the inner ply), retaining the crack tip opening determined from FEA, but dispensing with the delaminations. The calculated leak rates were found to be about 70% larger than experimental data, which was attributed to the presence of surface roughness in actual laminates, whereas the CFD model assumed smooth crack surfaces.

While the research discussed above has considerably advanced our understanding of the gas leakage mechanisms in CFRPs and provided useful empirical tools for estimating leak rate, significant gaps persist. Some major challenges include (a) existing gas-leakage models rely strongly on destructive or postmortem experimental data, which may not always be available, such as matrix cracking profiles at cryogenic temperatures; (b) there is a lack of multiscale modelling framework for determining the onset, growth, coalescence, and percolation of matrix cracks that control gas leakage. Existing cohesive-zone modelling provides a physically sound approach for calculating crack-tip opening displacements [23], and hence throat areas. However, implementation of CZM requires predefining potential crack paths for the purpose of inserting cohesive elements across the crack surfaces [24], which becomes impractical when the number and spacing of cracks themselves are unknown. In contrast, continuum damage mechanics (CDM) is widely used to simulate progressive matrix-dominated failure in full-scale laminates without discretizing every crack surface *a priori* [25, 26]. However, conventional CDM faces two key barriers for practical applications: (a) it requires a large set of ply-level strength and fracture-energy parameters, many of which are difficult to measure or lack standardized procedures, as highlighted in [25], and (b) it represents matrix cracking as a smeared band of damaged elements [27-29], which does not directly provide the explicit openings needed to quantify crack-intersection throat areas. Recently, micromechanical damage models (MDM) has been shown to address the first limitation by reducing the number of model parameters to a small set of constituent-level matrix and fibre–matrix interface material properties [25]. However, direct full-field MDM of a laminate model is computationally prohibitive due to the micron-scale resolution required to resolve fibres and interfaces [25, 30].

The present work aims to address these challenges by developing a new multiscale framework for predicting the percolation process of matrix cracks and gas leak rate in carbon fibre composites. The framework introduces a multiscale MDM–CDM strategy [25] to simulate the evolution of ply-wise crack density under biaxial loading and a parameter-scale and a scale bridging approach by a hierarchical homogenisation strategy. For each crack-density state obtained from the MDM–CDM model, the associated crack-intersection throat areas are computed using a computationally efficient unit cell model. Once the matrix crack densities and throat areas have been determined, the leak rate can be calculated by the approach originally presented in [7], which requires a discharge coefficient that, in general, must be determined empirically for a given laminate and damage state. However, it will be shown that a commonly employed value for the discharge coefficient for orifice flow [31-33] leads to predicted leak rates that agree well with the experimental data in [7, 18, 19], thereby providing a complete computational prediction for leak rates that effectively constitutes a digital twin capability for assessing leak rates across laminates. Compared with existing models for predicting leak rates

across matrix-cracked laminates, the proposed framework offer several advantages, including (a) a multiscale approach for calculating crack densities as a function of applied load, instead of relying on experimental data that may not be readily available, for example for matrix cracking at cryogenic temperatures, and (b) a unit cell model in which matrix crack planes and ply interfaces are modelled using a cohesive zone model (CZM) [23] to provide a physically consistent model of throat openings at matrix-crack intersections, under both thermal and mechanical loads, instead of relying on arbitrarily prescribed delamination lengths.

The proposed framework outlines an effective strategy to enrich CDM with MDM through parametric upscaling, thereby enabling full-scale laminate modelling while retaining constituent-informed fracture physics [25]. The remainder of this paper is structured as follows. Section 2 details the multiscale methodology for determining matrix crack densities and crack-intersection throat areas. Section 3 verifies several key aspects of the proposed modelling and experimental methods. Section 4 reports the predicted evolution of matrix crack density and compares these results with experiments. These predicted damage states are then employed to parameterize the cohesive-network unit cell model for predicting the leak rates at various load levels in Section 5. These predictions are compared with allowable leak-rate limits in existing standards to determine the leakage-threshold load at both room temperature (RT) and cryogenic temperature (CT). The merits and limitations of the present approach as a digital twin tool are briefly discussed in Section 6, followed by concluding remarks in Section 7.

2. Multiscale modelling framework

The aim of the proposed framework is to predict the two critical damage-state parameters required for through-thickness gas leakage modelling: (a) the matrix crack density in each ply, as a function of applied load, ε_{app}, and (b) the CTODs at crack-intersection throats, as noted in Section 1 and in Fig. 2. For this purpose, the present modelling approach includes two novel features relative to prior leakage analyses [7, 18-21]. First, the evolution of ply-wise crack density under biaxial loading is explicitly predicted using a multiscale MDM–CDM strategy [25] in Sections 2.1–2.2. Second, for each crack-density state obtained from the MDM–CDM model, the associated crack-intersection throat areas are computed using a computationally efficient unit cell model in Section 2.3. These inputs are then employed to predict leak-rate evolution with applied load via a compressible-gas orifice model described in Section 2.4. The flowchart in Fig. 3 schematically shows the outline of the proposed modelling framework. To facilitate direct comparison of present modelling results with reported biaxial tension and gas leakage measurements in [7, 18, 19], all simulations pertain to the IM600/#101 carbon-fibre/epoxy system [7, 18, 19], employing properties for IM600 fibres, #101 epoxy, and the fibre-matrix interface [25, 34], as summarized in Table 1.

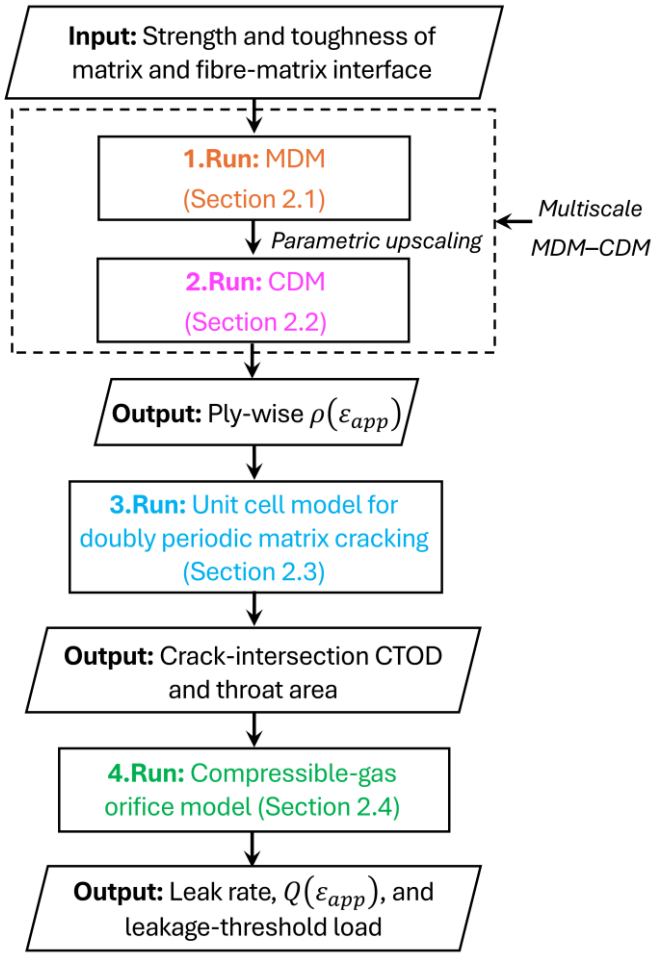

Fig. 3 Overall flowchart of the proposed multiscale modelling framework.

2.1 Micromechanical Damage Model

To significantly reduce the number of model parameters required by the continuum damage mechanics [25], a micromechanical modelling approach is developed by using a representative volume element (RVE) to explicitly analyse carbon fibres, matrix, and fibre–matrix interfaces, as shown in Fig. 4(a). The RVE dimensions, fibre distribution, and the minimum inter-fibre spacing are determined using a sensitivity method [25] to ensure statistically representative responses. Fibres are modelled as straight, transversely isotropic, linear-elastic solids. The epoxy matrix is described by a pressure-dependent elastic–plastic constitutive law with continuum damage and crack-band regularization [25], implemented in Abaqus/Explicit [35] via a user-defined VUMAT. The fibre–matrix interface is represented by zero-thickness cohesive elements with a coupled bilinear traction–separation law [25]. Interface damage initiates according to a stress criterion and evolves according to a mode-independent fracture energy G_{int}, consistent with experimental evidence that interface toughness is a small fraction of the bulk epoxy's toughness, i.e., $G_{int} = \beta G_{c,ep}$ with $\beta = 0.1$ in this work based on the experimental measurement in [25, 36]. The peak interface traction, S_{int}, is assumed to be equal to the matrix strength, as discussed in [25]. Unified periodic boundary conditions [25] are applied in all three principal

directions to enable homogenization under general multi-axial loading. Thermal residual stresses due to the difference between curing temperature and operating temperature are included by an initial thermal step prior to mechanical loading.

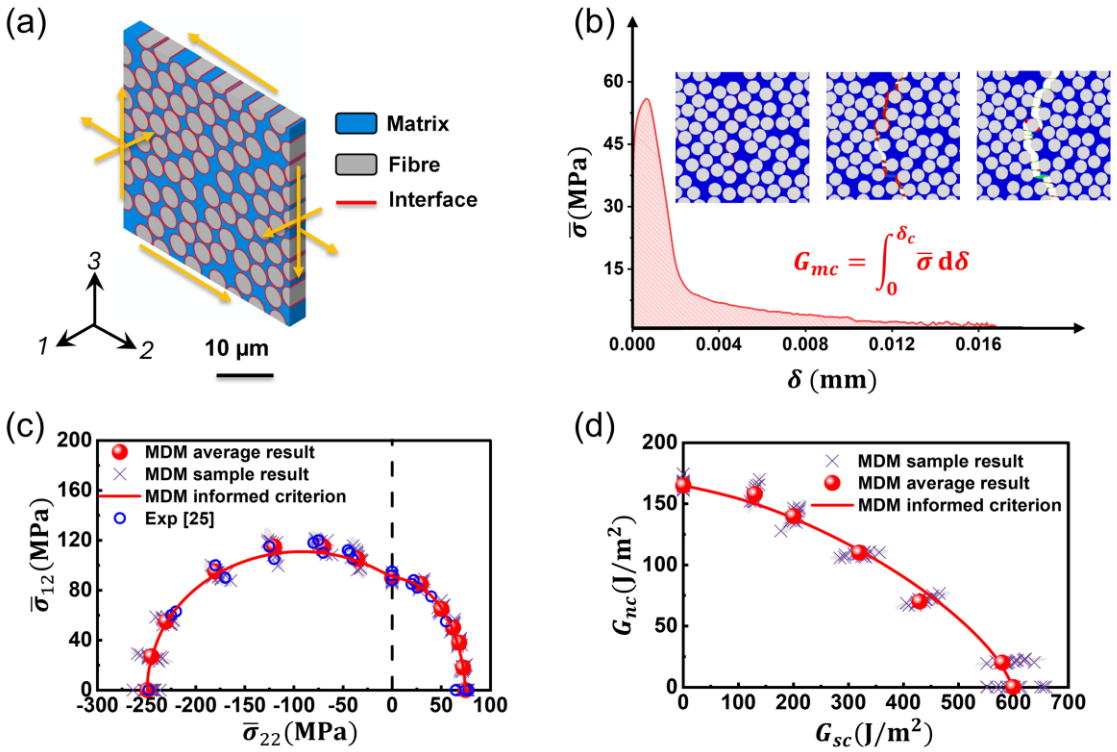

Fig. 4 MDM for matrix-dominate damage. (a) Micromechanical RVE of a CFRP ply under multiaxial loading states. (b) MDM computation of traction-separation relation under simple loading for matrix cracking. MDM-informed failure envelopes for (c) ply strength and (d) matrix-cracking fracture energy.

Computational simulations (digital twin) are then performed by prescribing normal and shear separations (Δu_n and Δu_s) to the RVE along loading paths with fixed mode-ratios $\lambda = \Delta u_s/\Delta u_n$ for different loading cases. All analyses are performed under quasi-static conditions using Abaqus/Explicit [35] with energy balance checks to ensure negligible spurious kinetic or hourglass energy. The average stresses along the unit cell edges and separations across the opposing edges of the unit cell are determined, which are then post-processed into size-independent traction–separation relations by decomposing the total separation into elastic and inelastic components; the latter defines the crack-band separations, as follows [25]:

$$\delta_n = \Delta u_n - \bar{\sigma}_n/K_n, \quad \delta_s = \Delta u_s - \bar{\sigma}_s/K_s, \tag{1}$$

where K_n and K_s denote the initial normal and shear stiffnesses of the RVE model, $\bar{\sigma}_n(\delta_n)$ and $\bar{\sigma}_s(\delta_s)$ represent the cohesive tractions. Fracture energies for a given mode are calculated as the area under the corresponding traction–separation curves, as depicted in Fig. 4(b) for matrix-cracking toughness G_{mc} under the pure normal loading. For mixed-mode loading, equivalent separation and traction measures are introduced [37],

$$\delta_{eq} = \sqrt{\delta_n^2 + \delta_s^2}, \quad \bar{\sigma}_{eq} = \sqrt{\bar{\sigma}_n^2 + \bar{\sigma}_s^2}, \tag{2}$$

so that each MDM simulation with a fixed λ gives an effective traction–separation curve $\bar{\sigma}_{eq}(\delta_{eq}; \lambda)$. By sweeping λ, the MDM generates strength and fracture-energy envelopes for matrix-dominated failure, as shown in Figs. 4(c, d), which are fitted with compact power-law relations, i.e., $\left(\frac{G_n}{G_{nc}}\right)^m + \left(\frac{G_s}{G_{sc}}\right)^m = 1$, to determine the mode-mixity coefficient, m,where G_n and G_s denote the denote the dissipated energy in the normal and shear directions; G_{nc} and G_{sc} the fracture energies for pure normal- and pure shear-mode failure, respectively. The complete traction–separation response is then represented using a power-law softening law parameterized by these cohesive strengths and fracture energies, providing a unified description over the range of prescribed mixed-mode boundary conditions applied to a single RVE. In this way, numerous ply-level strength/toughness quantities that would otherwise need to be determined experimentally or empirically for mesoscale ply-level modelling are instead derived directly from the MDM based on relatively few constituent properties as inputs.

Table 1 Material parameters for MDM

Carbon-fibre property	***Value***
Longitudinal Young's modulus (GPa)	260
Transverse Young's modulus (GPa)	15
In-plane Poisson's ratio	0.2
Longitudinal shear modulus (GPa)	15
Transverse shear modulus (GPa)	7
Coefficient of thermal expansion (K^{-1})	-7×10^{-7}
Coefficient of thermal expansion (K^{-1})	5×10^{-6}
Density (kg/mm^3)	1.78×10^{-9}
Epoxy matrix properties	***Value***
Young's modulus (MPa)	3760
Poisson's ratio	0.35
Plastic Poisson's ratio	0.3
Fracture energy, $G_{c,ep}$ (J/m^2)	300
Tensile strength (MPa)	76
Compressive strength (MPa)	300
Coefficient of thermal expansion (K^{-1})	45×10^{-5}
Curing temperature (℃)	120
Density (kg/mm^3)	1.3×10^{-9}
CZM parameters for the fibre-matrix interface	***Value***
Penalty stiffness (MPa/mm)	10^8
Peak traction (MPa)	76
Interfacial fracture energy, G_{int} (J/m^2)	30

Table 2 MDM-derived damage model parameters for CDM model

Property parameter	***MDM-derived value***
Ply strengths	
Transverse tensile strength, S_{2t}	56 MPa
Transverse compressive strength, S_{2c}	182 MPa
Through-thickness tensile strength, S_{3t}	56 MPa
Through-thickness compressive strength, S_{3c}	182 MPa
Longitudinal shear strength, S_{12}	82 MPa
Transverse shear strength, S_{23}	55 MPa
Fracture energies (kJ/m^2)	
Transverse normal (matrix cracking) toughness, G_{mc}	173 J/m^2
Transverse shear toughness (under pure τ_{12}), G_{sL}	605 J/m^2
Through-thickness normal toughness, G_{3n}	173 J/m^2
Through-thickness (under pure τ_{23}), G_{sT}	605 J/m^2
Mode-mixity parameter for matrix-dominated failure	Power-law m=1.4
Softening exponent, η	4.35

Table 3 Homogenized thermoelastic properties from MDM and comparison with measured values

Material property	*Experimental*	*MDM homogenization*
Young's moduli		
E_L (MPa)	147000 [18]	141068
E_T (MPa)	8700 [18]	8525
Poisson's ratio		
ν_L	0.3 [18]	0.27
ν_T	0.35 [18]	0.37
Shear moduli		
μ_L (MPa)	3900 [18]	4108
μ_T (MPa)	2300 [24]	2526
Coefficients of thermal expansion		
α_L ($^\circ$C^{-1})	-3×10^{-7} [34]	-3.2×10^{-7}
α_T ($^\circ$C^{-1})	22.8×10^{-6} [34]	21.9×10^{-6}
Density		
(kg/mm^3)	1.57×10^{-6} [34]	1.58×10^{-6}

2.2 CDM modelling of matrix crack densities

At the mesoscale, each ply is modelled as a homogeneous orthotropic solid. Matrix-dominated intralaminar damage (manifesting as matrix cracking under transverse tension) is represented using a crack-band CDM formulation, as shown in Fig. 5(a). Damage initiation at an element is governed by the MDM-derived strength envelope, evaluated using the element stresses $\sigma_{22}, \sigma_{23}, \sigma_{12}$. Damage evolution follows the MDM-derived traction–separation law, mapped to an element-level equivalent separation, $\Delta u_{eq} =$

$\sqrt{(L_e\langle\varepsilon_{22}\rangle)^2 + (L_e\varepsilon_{23})^2 + (L_e\varepsilon_{12})^2}$, where L_e is the characteristic element length. The corresponding equivalent elemental stress is defined by $\sigma_{eq} = \sqrt{\sigma_{22}^2 + \sigma_{12}^2 + \sigma_{23}^2}$. A scalar damage variable D is introduced such that the degraded response satisfies $\sigma_{eq} = (1 - D)K\,\Delta u_{\mathrm{eq}}$, and $D(\,\Delta u_{\mathrm{eq}})$ is selected to reproduce the MDM traction law while preserving the fracture energy through crack-band regularization, as illustrated in Fig. 5(a). This gives [25]:

$$D = 1 - \frac{\Delta u_0}{\Delta u_{eq}}\left(1 - \frac{\Delta u_{eq} - \Delta u_0}{\Delta u_c - \Delta u_0}\right)^{\eta} \tag{3}$$

where Δu_0 denotes the equivalent separation at damage onset, Δu_c the critical separation corresponding to complete loss of load-carrying capacity, and η the softening exponent. The required CDM parameters (ply strengths, fracture energies, and mode-mixity coefficient, and softening exponents) are taken from the MDM outputs, as summarized in Table 2, and implemented in Abaqus/Explicit [35] via a user-defined VUMAT. Other thermoelastic properties of the CFRP system are also derived from MDM and compared with experimentally measured values, as summarized in Table 3.

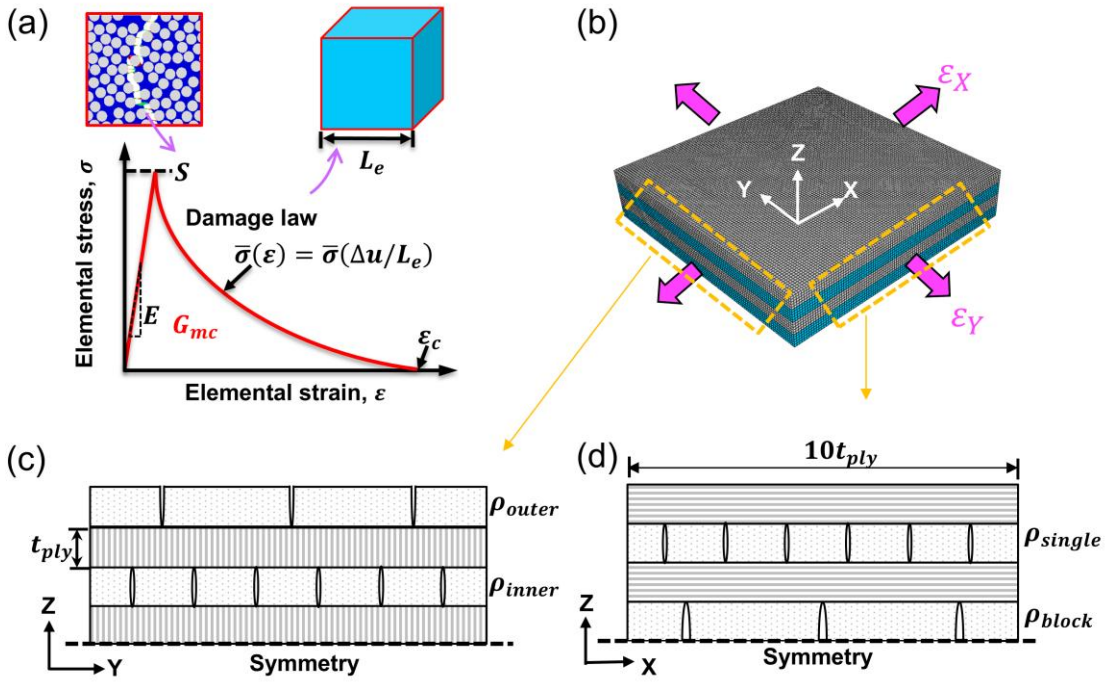

Fig. 5 Schematic of CDM and FE modelling of ply-wise matrix crack density under biaxial tension. (a) Crack-band approach used to embed the MDM-derived softening law into a CDM formulation at the element level. (b) 3D FE laminate CDM model subjected to biaxial loading to predict ply-wise matrix cracking evolution. (c,d) Schematic of *Y*–*Z* and *X*–*Z* plane views depicting the cross-ply layup and definitions of crack-density functions for four transverse-ply categories.

2.2.1 FE model of cross-ply laminates

The CDM formulation is applied to a 3D FE model of a square laminate region representative of the interior region of a large symmetric cross-ply laminate $[0/90/\,0/90]_S$ with nominal ply thickness $t_{ply} = 0.15$ mm, consistent with experiments reported in [19]. Half the laminate is modelled using a symmetry boundary condition at the mid-plane, as shown in Fig. 5(b). To sufficiently capture the crack density evolution and minimize edge effects, the in-plane dimension of the region is taken as ten times the layer thickness, and periodic boundary conditions are applied on the four faces to enforce in-plane deformation. Each ply is discretized using 3D solid elements (C3D8R). Mesh sensitivity is assessed by varying the ratio of ply thickness to element size from 1 to 9 (i.e., each ply is discretized by between 1 and 9 rows of elements in the thickness). Plies are linearly elastic prior to damage initiation. Interlaminar delamination is captured by cohesive surface elements inserted at all 0/90 interfaces, using the same MDM-informed traction–separation and fracture parameters such that matrix cracking and delamination are governed by a consistent matrix-dominated fracture description. Cure-induced residual stresses are included by applying an initial uniform thermal step of $\Delta T = -100°\mathrm{C}$ (from 120 °C to 20 °C) prior to mechanical loading. In this study, a matrix crack is identified as a contiguous band (in *Z*-axis direction) of fully damaged elements (with damage variable $D = 1.0$) spanning the full thickness of the ply or blocked-ply layer. Biaxial loading is achieved through periodic boundary conditions that apply prescribed uniform displacements to the reference nodes tied to the specimen faces, producing equi-biaxial strain $\varepsilon_X = \varepsilon_Y = \varepsilon_{app}$ for the laminate. The matrix crack density, ρ, is defined as the number of matrix cracks in a transverse ply per unit length from the observing view plane. Figs. 5(c,d) distinguish four crack density functions analysed in this study: ρ_{block} and ρ_{single} for a block of two-ply layer and single ply in *X*-*Z* view plane; ρ_{inner} and ρ_{outer} for inner embedded and outer plies in *Y*-*Z* view plane. The resulting $\rho(\varepsilon_{app})$ data are presented later in Section 4 to validate the equi-biaxial MDM–CDM predictions of matrix crack density evolution.

2.3 Unit cell model for doubly periodic matrix cracking

The pattern of matrix cracking in a cross-ply laminate under equi-biaxial loading can be regarded as being periodic in two orthogonal directions (i.e. doubly periodic), as a reasonable approximation, as indicated in Fig. 6(a). The average crack spacing for a given applied load level is determined from the crack density derived through the MDM–CDM approach in Sections 2.1–2.2. In view of the assumed periodicity, a computationally efficient approach for determining the throat areas at interply crack intersections is to employ a unit cell model whose in-plane dimensions correspond to the average crack spacing, as shown in Fig. 6(a), and as previously employed in [22]. However, unlike the previous work in [22], where delaminations of varying length were

arbitrarily inserted at the tips of through thickness matrix cracks, to ensure a non-zero crack tip opening at the interface, the present work employs a CZM for the interface, which provides a mechanically sound approach for determining the crack tip opening, and hence the throat area, at the interface. As shown in Fig. 6(a), the unit-cell model represents a symmetric cross-ply laminate patch, constructed as a repeating unit cell consistent with the laminate architecture described in Section 2.2, i.e., $[0/90/0/90]_S$. Periodic boundary conditions are applied on the four faces. The composite plies are modelled as homogeneous orthotropic solids using 3D, 8-node, linear brick element with reduced integration and hourglass control (i.e., C3D8R elements) and are assumed linearly elastic. Matrix cracks are assumed to occur in a uniformly distributed (i.e., periodically spaced) pattern within each layer. The unit-cell dimensions are then selected such that the model contains one representative repeat segment of the periodic crack pattern in each cracked layer, as depicted in Fig. 6(a). Zero-thickness cohesive elements available in Abaqus [35] are pre-inserted along the intralaminar planes where matrix cracking is assumed to occur as well as the ply interfaces for interlaminar delamination. The CZM parameters follow those established in Sections 2.1–2.2 and summarized in Table 2, ensuring a physically correct fracture description for both matrix cracking and interlaminar delamination. For each prescribed crack-density state, the unit cell is loaded in equi-biaxial in-plane tension up to the corresponding strain level, as determined in Section 2.2. A representative damage contour for cohesive elements at a crack intersection under $\varepsilon_{app} = 1\%$ is shown in Fig. 6(b). The CTOD is then taken as the crack-opening displacement evaluated at the ply interface. As shown in Fig. 6(c), the throat created by the intersection of matrix cracks in adjacent plies is a rectangular opening, whose side lengths are given by the CTODs of the two intersecting matrix cracks. Thus, for an intersection between k_{th} and $(k+1)_{th}$ plies, the crack-intersection throat area is $A_k = \Delta_k \Delta_{k+1}$. Repeating this calculation for all intersection points within the unit cell yields the effective throat area required by the compressible-gas orifice model described below.

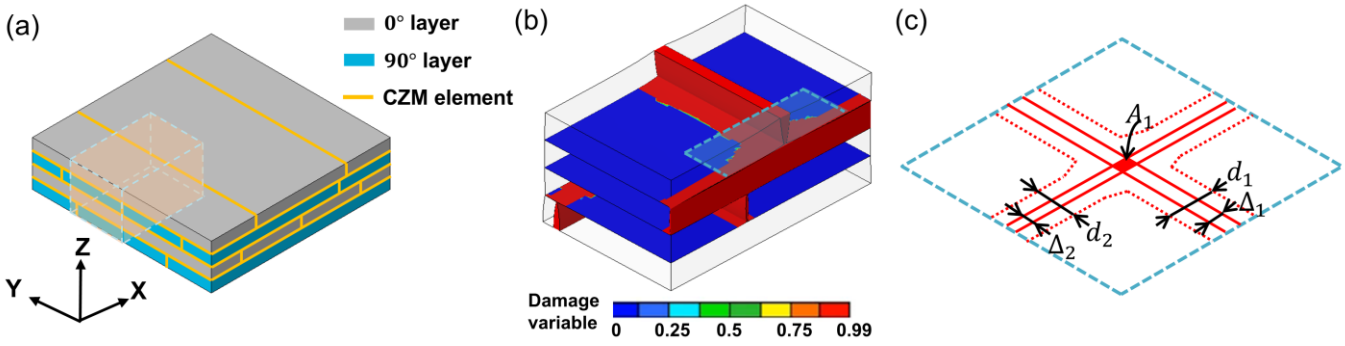

Fig. 6 Unit-cell model of doubly periodic matrix cracking for computation of crack-intersection CTOD and throat area. (a) Model configuration of the cohesive network. (b) An example damage contour plot showing intersecting matrix cracks and delamination around a crack intersection throat. (c) Plan-view definition of the crack-intersection throat geometry for the computation of throat area A_1 from the CTODs, Δ_1, Δ_2.

2.4 Compressible-gas orifice modelling of leak rate through damaged laminates

Having determined both the crack density in all layers and the crack-tip openings at the interfaces, one can next calculate the leak rate, Q, across a damaged laminate by adopting the approach originally proposed by Kumazawa et al. [7] in which Q is proportional to the pressure drop across the laminate, as follows:

$$Q = C\frac{(P_u - P_d)}{P_{ref}}\frac{T_{ref}}{T}, \tag{4}$$

where C denotes the laminate conductance, P_u and P_d are the upstream and downstream absolute pressures, T is the gas temperature, and P_{ref}, T_{ref} denote a prescribed reference pressure and temperature, which are here chosen to be $1\ \text{atm}, 25℃$ to match the experimental conditions in [7, 18, 19]. The laminate conductance per unit area can be calculated using a compressible-gas orifice model [38]:

$$C = C_d A_{eff}\sqrt{\gamma R_s T}\left(\frac{2}{\gamma+1}\right)^{\frac{\gamma+1}{2(\gamma-1)}}, \tag{5}$$

where C_d is the discharge coefficient, R_s is the specific gas constant, γ is the heat-capacity ratio of the gas, and A_{eff} is the effective throat area per unit laminate area which is obtained as follows.

For the interface between the k_{th} and $(k+1)_{th}$ layers, the number of crack intersections per unit laminate area at any given load level is $\rho_k\rho_{k+1}$, and the throat area of an individual intersection is idealized as a rectangle with area $\Delta_k\Delta_{k+1}$. The effective throat area fraction for the interface is therefore $\rho_k\rho_{k+1}\Delta_k\Delta_{k+1}$. Using the reciprocal formula for series conductance through the various throats across the thickness, one obtains

$$A_{eff} = \left(\sum_k \frac{1}{\rho_k\rho_{k+1}\Delta_k\Delta_{k+1}}\right)^{-1}. \tag{6}$$

Combining Eqs. (4-6) yields the leak rate for a given load level. For a specified gas and temperature, γ and R_s are known in engineering handbook [39], whereas the appropriate value for the discharge coefficient should, in principle, be determined empirically for each laminate and load level. However, for regularly shaped sharp-edged orifices, C_d values ranging from 0.60 to 0.63 are commonly reported [31-33, 40] across a wide range of Reynolds number, Re. Accordingly, a median value of $C_d = 0.615$ is adopted in this work. The validity of this choice for C_d will be further discussed in Section 6.

3 Verification of MDM-CDM-CZM model

3.1 Effect of mesh size on CDM predictions of matrix crack density

Mesh sensitivity of the MDM–CDM model was assessed under equi-biaxial tensile loading. Fig. 7(a) shows predicted evolution of matrix crack density of the block layer, ρ_{block}, as a function of the applied strain ε_{app}

for different element sizes, expressed as the ratio t_{ply}/L_e. The stress for the first matrix-cracking event is essentially mesh-independent, with all curves in Fig. 7(a) start rising within a narrow stress band around $\varepsilon_{app} \approx 0.63\%$. This mesh insensitive behaviour is attributed to the crack-band formulation which enforces the correct fracture energy for a single localized damage band, making the onset of localization largely independent on element size. In contrast, the subsequent evolution of crack density is strongly mesh-dependent for coarse meshes. When only one or two elements are used through a ply thickness, each element row acts as a wide smeared crack band; once damage localizes, additional cracking can only be represented by widening the existing damage band rather than forming multiple distinct crack-band zones. This leads to step-like $\rho - \varepsilon_{app}$ curves. With mesh refinement to $t_{\mathrm{ply}}/L_e \geq 5$, the $\rho - \varepsilon_{app}$ curves nearly coincide, indicating convergence and a smeared-crack representation that more closely approximates a family of discrete matrix cracks. This converged refinement level is also consistent with prior MDM-to-CDM comparisons [25] showing that around five solid elements per ply allows damaged-element bands to be interpreted as equivalent cracks at practical computational cost. This indicates that the converged element length is commensurate with the effective fracture-process zone size at a matrix crack tip near the interface [41]. Accordingly, $t_{\mathrm{ply}}/L_e = 5$ (i.e., $L_e = 30$ μm) is adopted in the remainder of this paper for the CDM as well as the cohesive-network unit cell modelling.

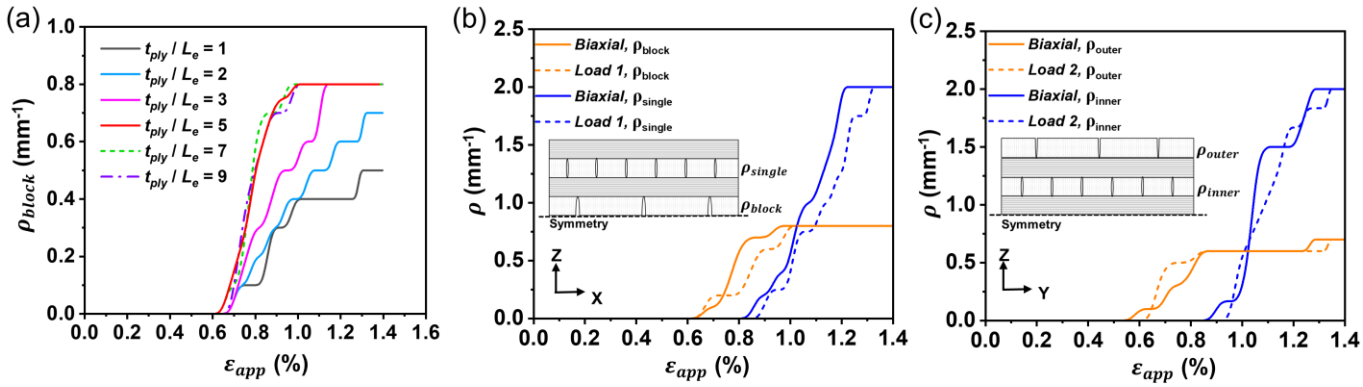

Fig. 7 Verification of the MDM–CDM modelling of matrix crack density. (a) Effect of FE mesh size L_e on the predicted ρ_{block} versus ε_{app} under equi-biaxial loading. Comparison of predicted crack density evolution, $\rho(\varepsilon_{app})$ curves, for various transverse ply categories under equi-biaxial loading (solid lines) with sequential uniaxial Loading 1 in (b) and with Loading 2 in (c).

3.2 Comparison between equi-biaxial and sequential uniaxial tension

While biaxial tension is the most representative loading condition for interrogating leakage-relevant matrix cracking in CFRPs, it is experimentally demanding, and challenges may be further exacerbated at cryogenic temperatures. To assess whether biaxial loading can be adequately simulated by sequential uniaxial loading,

the following loading path is also investigated computationally: (a) *Load 1*: uniaxial loading in *X* direction to a prescribed strain $\varepsilon_X = \varepsilon_{app}$ with the *Y* direction traction free, followed by complete unloading; and then (b) *Load 2*: uniaxial loading in *Y* to the same $\varepsilon_Y = \varepsilon_{app}$ with the *X* direction traction free. Predicted ply-wise matrix crack density evolutions for the four transverse-ply categories are compared in Fig. 7(b,c). It can be seen that matrix cracking initiates at a slightly lower ε_{app} under the equi-biaxial loading, but the difference in onset stress remains modest (within 13%). More importantly, the subsequent evolution of matrix crack densities is nearly identical for equi-biaxial loading relative to sequential uniaxial loading. The difference in crack densities at a given level of ε_{app} remains below about 10%. This indicates that, once matrix cracking has occurred, the progression and final extent of matrix-cracking density are largely insensitive to whether the cross-ply laminate is loaded simultaneously or sequentially in the two in-plane directions.

This similarity arises for cross-ply laminates because matrix cracking is matrix-dominated and only weakly perturbs the laminate in-plane stiffness; hence, matrix damage accumulated during Loading 1 has little influence on the stress redistribution during Loading 2. This weak coupling is consistent with classical laminate theory [42] for symmetric cross-ply laminates, where the coupling stiffness A_{12} (and thus the effective laminate Poisson's ratio) is small, so that sequential uniaxial loading closely reproduces the biaxial damage state. These results indicate that sequential uniaxial testing represents a feasible and attractive experimental route for future validation of equi-biaxial matrix-cracking predictions for cross-ply laminates, particularly where true biaxial testing at cryogenic temperatures is not readily achievable.

3.3 Matrix crack COD profiles and CTODs at crack intersections

Fig. 8 benchmarks the proposed cohesive-network unit-cell model (Section 2.3) as a practical route to compute the CTOD at crack intersections, as required for leakage modelling. Fig. 8(a) compares the through-thickness COD profile, $COD(z)$, for a matrix crack in the block layer under equi-biaxial tension at $\varepsilon_{app} = 1\%$. Using the converged discretization $t_{\text{ply}}/L_e = 5$ as determined in Section 3.1, the cohesive-network prediction (red solid curve) is compared with a 2D sublaminate MDM result (dashed curve), which exhibits small fluctuations due to the random fibre distribution and the resulting heterogeneous debonding/matrix cracking as shown in Fig. 8(a). In the CDM laminate model, the matrix crack is represented as a band of fully damaged elements (see Fig. 9) and therefore does not provide an explicit opening; an effective COD is instead reconstructed by interpreting this damaged band as an equivalent discontinuity and computing the increase in transverse nodal spacing across the band relative to the undeformed element length (purple solid curve). The three COD profiles show good overall agreement in both shape and magnitude, indicating that the cohesive-network unit cell captures the through-thickness displacement field and stress redistribution induced by matrix cracking. Fig.

8(b) further highlights its computational advantage. On a 56-core Intel Xeon (1.9 GHz), the cohesive-network analysis is approximately six times faster than the CDM laminate simulation and forty times faster than the 2D-MDM for obtaining the COD profiles shown in Fig. 8(a).

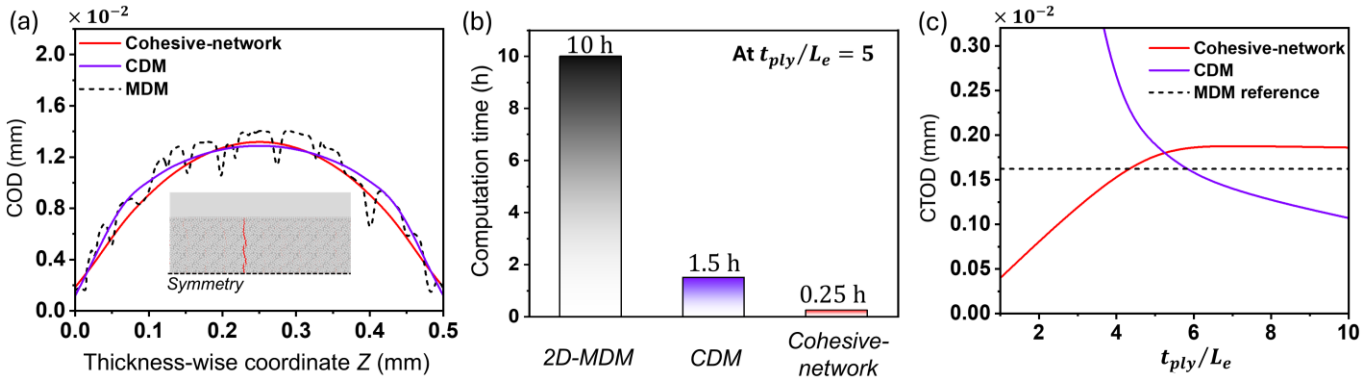

Fig. 8 Predictions of matrix crack opening and computational efficiency for the cohesive-network unit-cell model. (a) Through-thickness COD profiles by the cohesive-network unit-cell model, CDM laminate model, and 2D MDM sublaminate model (shown as inset) at $\varepsilon_{app} = 1\%$. (b) Computation time for the three approaches. (c) Mesh sensitivity of CTOD predictions showing convergence of the cohesive-network prediction relative to the MDM reference and persistent mesh dependence for CDM.

The key motivation for using the cohesive-network model, however, is to obtain a reliable local CTOD for calculating the crack-intersection throat area in a computationally efficient way. Although the overall COD profiles are comparable among different approaches, Fig. 8(c) shows that CTOD inferred from the CDM laminate model is strongly mesh dependent over the investigated range, even though the matrix crack density prediction has already converged, highlighting the limitation of extracting the local crack-intersection opening from a smeared damage-band representation. By contrast, the cohesive-network CTOD converges for $t_{\text{ply}}/L_e \geq 5$, consistent with established CZM mesh-objectivity guidance [43], and the converged CTOD value is within 10% of the MDM reference value at a substantially lower computational cost. Accordingly, coupling the MDM–CDM's crack-density prediction with the cohesive-network unit-cell model provides an efficient and robust route to CTOD and throat area evaluation while retaining consistency with the laminate-scale damage response.

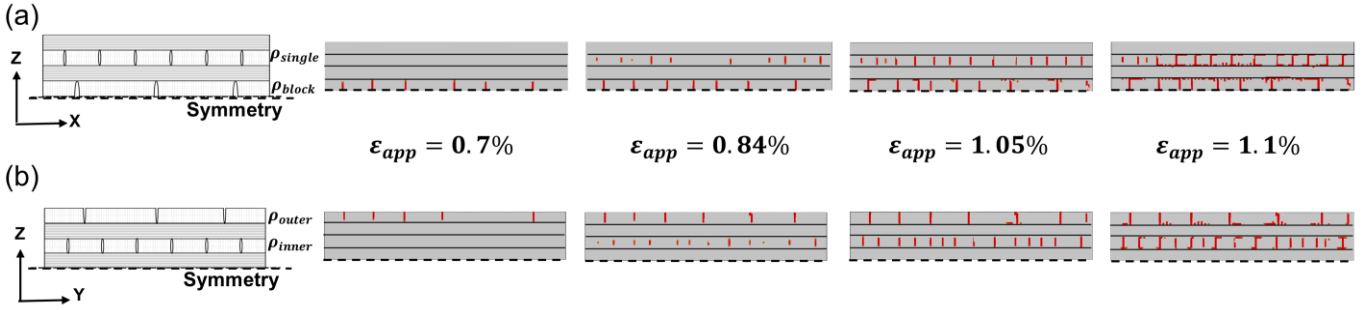

Fig. 9 Through-thickness matrix damage patterns predicted by the FE laminate model under equi-biaxial tension at various levels of ε_{app}. Cross-sectional views in (a) *X-Z* plane and (b) *Y-Z* plane.

4 Predicted matrix cracking under equi-biaxial load

4.1 Matrix crack densities at room temperature and comparison with experiments

Fig. 10 compares the MDM–CDM predictions of matrix crack density ρ with the equi-biaxial tension measurements reported by Kumazawa et al. [19] at room temperatures (RT). The model predictions at RT are shown as solid curves for the four transverse-ply categories defined in Section 2.2.1 (see insets of Fig. 10). Here, ρ is reported in mm^{-1} as a function of the applied laminate strain, ε_{app}. The intersection of each $\rho - \varepsilon_{app}$ curve with $\rho = 0$ provides the predicted onset strain for matrix cracking in the corresponding ply. Symbols in Fig. 10 represent measured crack densities from C-scan radiography observations [19], which indicate that matrix cracks always span the specimen width, thereby resulting in ply splitting.

Overall, the MDM–CDM predictions show excellent agreement with the experimentally observed crack-density evolution, capturing both the onset strains and the subsequent crack-multiplication trends with increasing ε_{app}. The predicted sequence of matrix cracking is also consistent with observations: under equi-biaxial loading, matrix cracking initiates first in the outer ply, followed by the middle block layer. At higher applied strains, however, the inner and single transverse plies develop systematically higher crack densities than the outer and block plies, typically by a factor of around 1.5, reflecting the layer-dependent stress redistribution and constraint within the cross-ply architecture. Collectively, these results validate the MDM–CDM framework for predicting the ply-wise matrix crack density in cross-ply laminates under biaxial loading at RT, providing the basis for extending the same modelling strategy to cryogenic temperatures in Section 4.2.

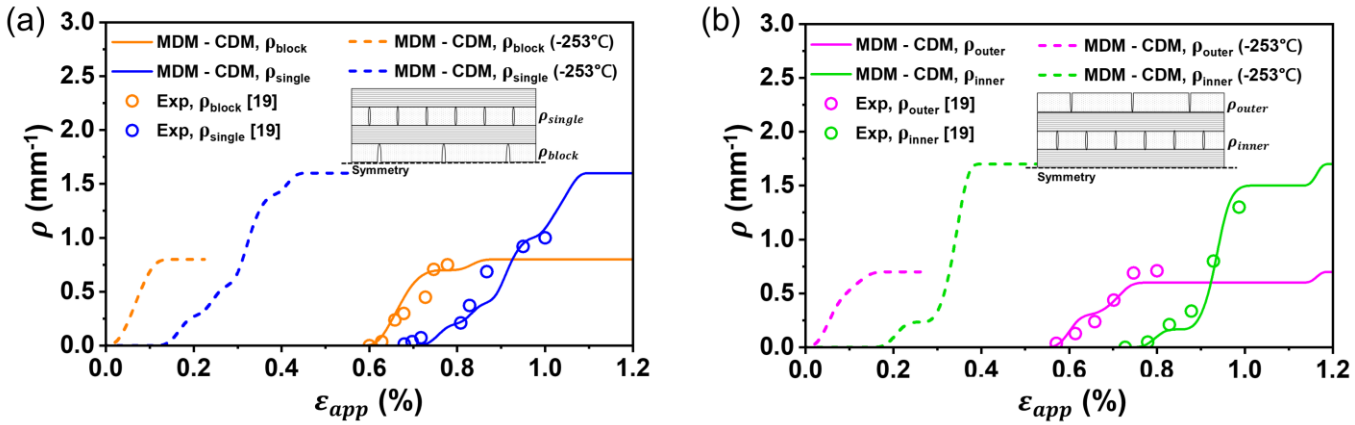

Fig. 10 Comparison of predicted $\rho - \varepsilon_{app}$ results with experimental measurements [19] for (a) ρ_{block} and ρ_{single}; (b) ρ_{inner} and ρ_{outer}. Predictions for cryogenic matrix cracking are shown by dashed curves, for which the matrix toughness, $G_{c,ep}$, is assumed to be 50% of that at room temperature.

4.2 Matrix crack densities at cryogenic temperatures

Cooling a CFRP laminate to cryogenic temperatures (CT) introduces substantially higher thermal residual stresses at two interconnected length scales [34]. At the intra-ply scale, residual stresses arise between fibres and matrix because of their mismatched coefficients of thermal expansion (CTEs). At the inter-ply scale, residual stresses arise between plies of different orientations within a laminate, due to the variation in the homogenized CTE relative to fibre orientation. To reflect a representative cryogenic tank scenario, the simulations in this section apply a temperature drop of $\Delta T = -373°\mathrm{C}$, corresponding to cooling from the curing temperature of $120°\mathrm{C}$ to liquid-hydrogen temperature of $-253°\mathrm{C}$. This thermal step is applied consistently in both the MDM (in Section 2.1) and the laminate-scale CDM model (in Section 2.2), so that the subsequent equi-biaxial loading is superposed on the thermal residual stress field.

In addition to the residual stresses, temperature-dependent fracture properties, particularly the matrix fracture toughness, are expected to strongly influence matrix-dominated damage at cryogenic temperatures, whereas variations in matrix and interface properties would be expected to be less critical. Specifically, the epoxy toughness is assumed to reduce from its RT value of $G_{c,ep} = 300\ \mathrm{J/m^2}$ to a CT value of $G_{c,ep} = 150\ \mathrm{J/m^2}$, a 50% reduction consistent with our prior experimental measurements [44-46] and modelling investigations [47, 48], while the fibre–matrix interface toughness is scaled proportionally, i.e. $G_{int} = \beta G_{c,ep}$ with $\beta = 0.1$ as noted in Section 2.1 and in [25]. All other properties are retained at their RT values for simplicity, so the modelling results in this section primarily reflect the combined effects of cooldown-induced residual stresses and reduced matrix toughness. The resulting predictions are shown as the dashed $\rho - \varepsilon_{app}$ curves in Fig. 10 Relative to RT, the onset of matrix cracking occurs at significantly lower applied strain, and crack densities grow earlier with increasing ε_{app}. This shift of the matrix cracking response directly reflects the fact that the laminate enters mechanical loading with substantial inter-ply residual strain, which is independent of internal pressure and therefore represents an intrinsic challenge for cryogenic CFRP vessels.

5 Predicted through-thickness gas leak rate

5.1 Helium leak rate at RT and comparison with experiments

To validate the proposed through-thickness leakage modelling framework, we benchmark it against the helium leak-rate measurements of Kumazawa et al. [7, 18, 19]. For direct comparison, the material system, laminate configuration, and biaxial loading conditions are set to follow Kumazawa et al. [7]. Specifically, the laminate is an IM600/epoxy cross-ply $[0_2/90_2]_S$ composite, as shown in Fig. 11(a), and an initial thermal step from 120 °C to 20 °C prior to mechanical loading is set for consistency with the experiments conducted at RT. The

present modelling replicate the same two-step "damage-then-leak" procedure as reported in [7, 18, 19]: the laminate is first loaded under equi-biaxial tension to $\varepsilon_X = \varepsilon_Y = 0.61\%$ to generate matrix cracks (with $\rho = 0.1\ mm^{-1}$ from the MDM–CDM and prescribed in the unit-cell model shown in Fig. 11(a)), fully unloaded, and then reloaded to $\varepsilon_{X,reload} = 0.25\%$ at biaxiality ratios $\varepsilon_{Y,reload}/\varepsilon_{X,reload} = -0.2, 0.31$ and 1, during which the leak rate was measured in [7, 18] and is modelled here for comparison. Because *in-situ* leak-rate measurements during progressive damage accumulation under true biaxial loading are experimentally challenging and remain lacking in the literature, available data are typically obtained either after unloading from a prescribed maximum load or during a low-level reloading stage where no additional damage develops. Accordingly, we compare the predicted leak rate during reloading directly with the measurements across various biaxiality ratios, aiming to provide a stringent validation of the present damage-to-leakage modelling approach.

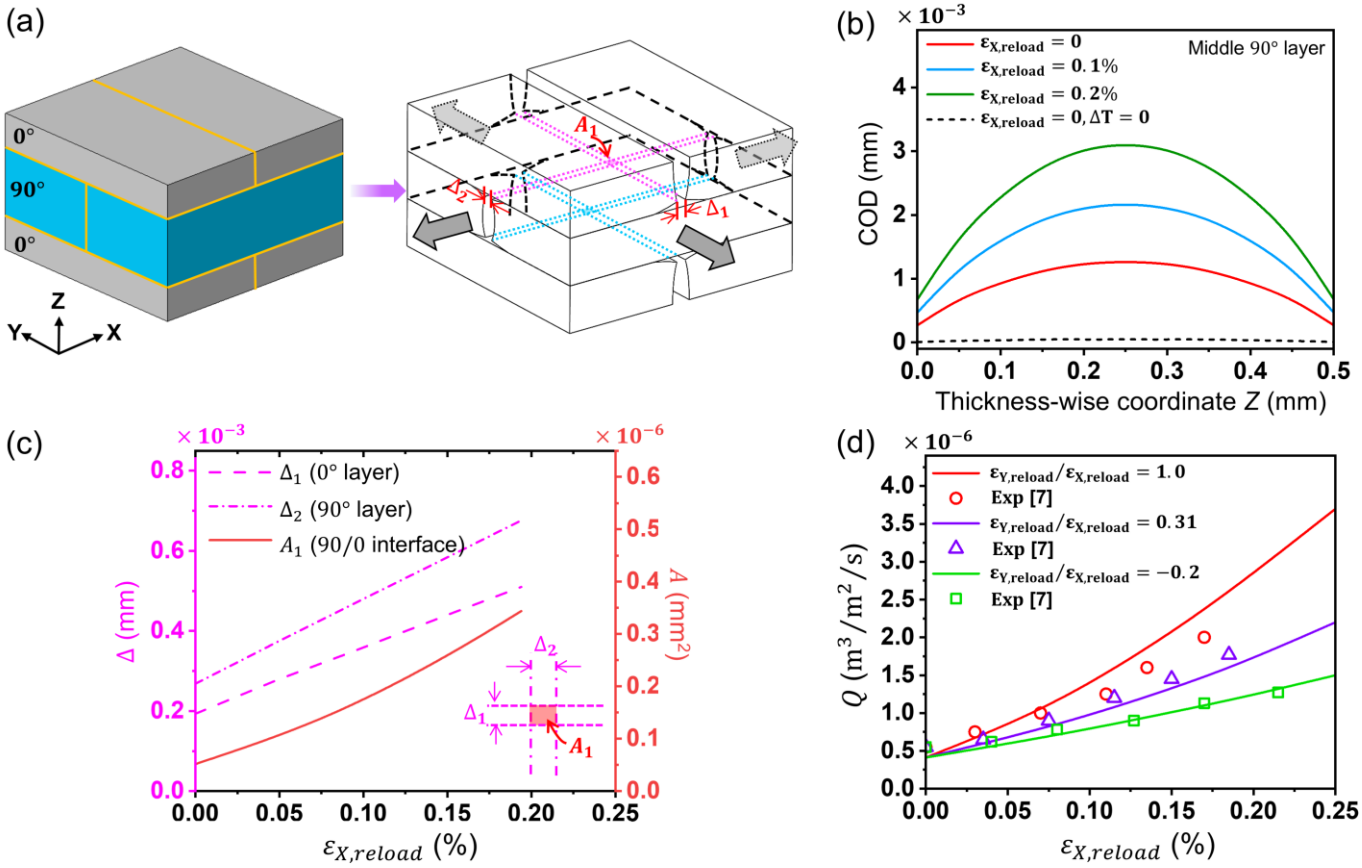

Fig. 11 Validation of the leak-rate modelling by comparing with helium leakage measurements for $[0_2/90_2]_S$ laminates in [7]. (a) Cross-ply laminate unit cell highlighting the cohesive-network modelling and illustration of the crack intersection. (b) Predicted COD profile by cohesive-network modelling, through the thickness of the middle 90° layer, at complete unload and during equi-biaxial reloading. (c) Predicted CTODs in the intersecting 0° and 90° layers and the resulting intersection throat area as functions of re-applied strain. (d) Predicted helium leak rate for various reloading biaxiality ratios, compared with experimental measurements in [7].

The computed COD profiles across the thickness of the middle block 90° layer are shown in Fig. 11(b) for the fully unloaded state and for the subsequent equi-biaxial reloading. The intersection of each profile with the vertical axis indicates the value of the CTOD, Δ_2, at the crack-intersection throat. Notably, at complete unload $\varepsilon_{X,reload} = 0$ the CTOD remains non-zero, whereas it becomes negligible only when the initial thermal step is suppressed by setting $\Delta T = 0$ (as shown by the dashed curve in Fig. 11(b)), indicating that the residual crack opening can be attributed to thermal residual stresses. The resulting CTODs for the intersecting 90° and 0° plies are plotted in Fig. 11(c) and increase approximately linearly with the re-applied strain; consequently, their product, representing the crack-intersection throat area, shows a quadratic dependence on strain. Using Eqs. (4–6) in Section 2.4, the predicted helium leak rate is shown in Fig. 11(d) for $\varepsilon_{Y,reload}/\varepsilon_{X,reload} = 1$, and for additional biaxiality ratios of 0.31 and -0.2 (the latter corresponding to uniaxial tensile reloading). Across all biaxiality ratios, the model shows excellent agreement with the measured helium leak rate through the matrix cracked laminates.

5.2 Hydrogen leak rate under biaxial load at RT and CT

Building on the validation in Sections 4 and 5.1, the framework is next applied to predict the *in-situ* hydrogen leak rate Q under equi-biaxial tension for the $[0/90/\,0/90]_S$ cross-ply laminate (for which the matrix-crack density evolution was quantified in Sections 3 and 4). Figure 12(a) plots the predicted $Q - \varepsilon_{app}$ response for three cases: (a) the RT baseline, (b) $-253°\mathrm{C}$ with reduced matrix toughness $G_{c,ep} = 150\ \mathrm{J/m^2}$, and (c) $-253°\mathrm{C}$ assuming a hypothetical toughened matrix with $G_{c,ep} = 300\ \mathrm{J/m^2}$, with the cryogenic modelling setup following Section 4.2. The logarithmic view in Fig. 12(b) also includes the diffusion-controlled permeation baseline, Q_{diff}, measured for pristine laminates and for laminates containing only isolated matrix cracks [7-9]. Once a through-thickness crack network forms, the leak rate is predicted to increase abruptly by several orders of magnitude relative to the diffusion baseline, consistent with observations in the literature and marking the onset of gas percolation [7, 8]. Such a step change in Q represents a transition in gas-transport mechanism from diffusion-controlled permeation to mass flow through an interconnected crack network. Accordingly, the gas-percolation threshold strain, ε_{cp}, can be identified at the onset of this abrupt deviation from Q_{diff}, giving $\varepsilon_{cp} = 0.93\%$ at RT, and a markedly lower value of $\varepsilon_{cp} = 0.33\%$ at $-253°\mathrm{C}$ for case (b). This shift at cryogenic temperature is consistent with the earlier onset and accelerated accumulation of matrix cracking predicted in Section 4.2 due to the combined effects of thermal residual stresses and reduced matrix toughness. Case (c) featuring a hypothetical toughened matrix leads to a significantly enhanced gas percolation threshold of $\varepsilon_{cp} = 0.48\%$ at $-253°\mathrm{C}$, indicating the potential benefit of emerging matrix nano-toughening techniques for improving the gas percolation threshold at CT [44-46].

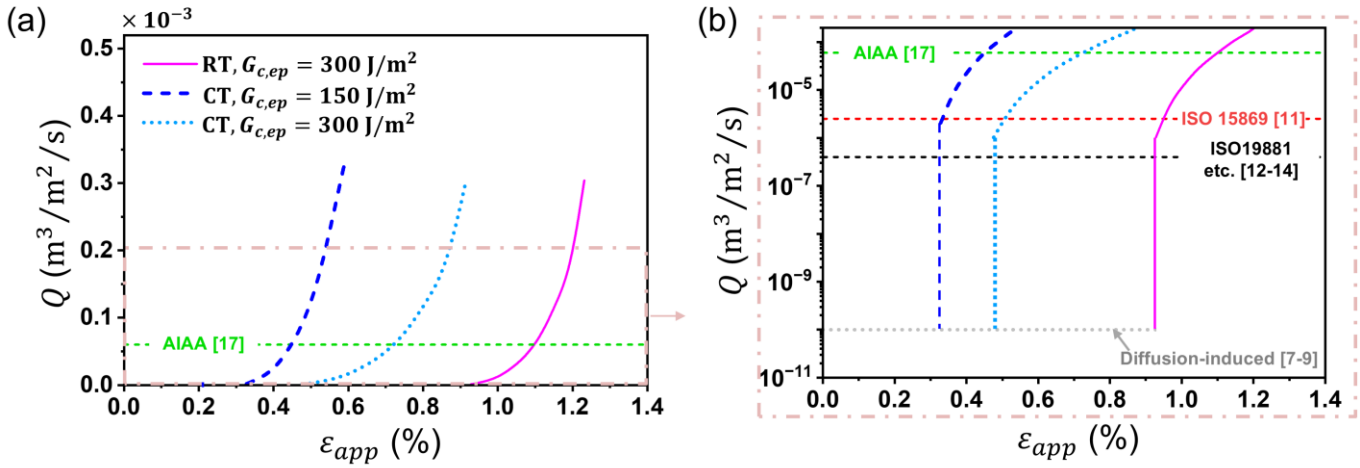

Fig. 12 Predicted *in-situ* hydrogen leak rate under equi-biaxial load for $[0/90/0/90]_S$ cross-ply laminates at RT and CT. (a) Linear scale Q–$\varepsilon_{\mathrm{app}}$ response compared with the allowable leak-rate limit from AIAA guideline [17]. (b) Zoomed plot on a logarithmic Q scale showing the diffusion-controlled leakage baseline measured in [7-9] and comparisons with representative allowable leak-rate limits from existing standards [12-14].

Furthermore, Fig. 12 enables direct determination of the leakage-threshold strain, ε_{lt}, defined by the intersection of the predicted $Q(\varepsilon_{app})$ curve with the allowable leak-rate limit, Q_{lim}. Considering the AIAA guideline limit for launch-vehicle LH_2 tanks [17], shown in Fig. 12, the predicted thresholds are $\varepsilon_{lt} = 1.09\%$ at RT, decreasing to $\varepsilon_{lt} = 0.44\%$ at $-253°C$ for degraded matrix, but retaining a relatively high value of $\varepsilon_{lt} = 0.73\%$ for the hypothetically toughened matrix system. The more stringent on-road limits [12-14] shown in Fig. 12(b) are exceeded at (or very shortly after) the percolation transition, whereas diffusion-controlled permeation remains well below all limits.

6 Discussion

The present work establishes a novel multiscale framework for simulating the percolation process of matrix cracks and leak rate in fibre-reinforced polymeric composites. It introduces several major innovations that lead to a predictive, mechanics-based digital twin framework. First, a multiscale micromechanical damage model (MDM) enriched continuum damage method (CDM) is developed to determine matrix crack densities in individual plies as a function of the multiaxial load (see Fig. 10), rather than being prescribed in existing methods from post-mortem observations. Second, a scale-bridging strategy is introduced using hierarchical homogenisation strategy to quantify the crack-intersection CTODs and resulting throat geometry required by the multilayer orifice gas flow calculation. This is resolved directly using a doubly periodic cohesive-network unit cell (see Fig. 11), rather than relying on a trial-and-error approach for determining an appropriate delamination size based on only one load case (the zero applied load case). The employed MDM-CDM approach reduces reliance on extensive independently measured ply-level strength and fracture energy inputs,

an issue that becomes particularly acute at cryogenic temperatures where diverse failure modes interact nonlinearly and standardized coupon testing methods are lacking [25]. In parallel, the mesh-refinement study (see Fig. 7) establishes a practical element-size guideline under which the CDM crack-band representation converges to a reliable surrogate for discrete matrix cracks, addressing a common concern with smeared continuum damage formulation in representing explicit cracks in CFRP laminates. Compared with discrete damage modelling (DDM) that typically require prescribed crack paths and heavy enrichment of the FE mesh [28], the present MDM-CDM strategy remains computationally efficient for ply-wise crack density calculation via a full-field laminate simulation, while providing high-fidelity local crack opening needed for leak-rate prediction through a physically consistent coupling to a computationally efficient cohesive-network unit cell model (see Fig. 8).

These improvements for calculating the throat areas are coupled in the present work with the discharge coefficient C_d in the throat conductance model originally proposed by Kumazawa et al. [7], given by Eq. (5), thereby providing a complete autonomous prediction of gas leak rates that does not require any empirical calibration. Thus, the present modelling approach can be considered to constitute a digital twin capability that should prove valuable for reducing the design iteration and certification costs for all-composite pressure vessels, particularly those that are required to operate at cryogenic temperatures [49].

The current choice of $C_d = 0.615$ falls within the range $C_d \approx 0.6 - 0.7$ that has been shown to predict measured micro-orifice flow rates within a few percent error over a wide range of Reynolds number (Re), including separated- and reattached-flow regimes [32, 33]. In the specific context of cracked CFRP laminates, Kumazawa and Whitcomb [22] reported that CFD simulations assuming perfectly smooth crack faces overestimated experimental leak rates by 70%. Interpreted through the orifice framework, this discrepancy corresponds to an effective discharge coefficient of 0.59, which aligns closely with commonly reported engineering values (i.e., 0.60–0.63 [31, 39, 40]). Furthermore, varying C_d within 0.59-0.68 alters the prediction results by only about ±6.5% (see Eq.5). Thus, the adopted value $C_d = 0.615$ can be considered a pragmatic choice vindicated by the good agreement with measured helium leak rates under various biaxial loading ratios (see Fig. 11). Nevertheless, it is noted that Re is of order-unity [50] in the present context, falling far below the range investigated in [32] (i.e., Re = 1000 to 7000), where a constant C_d of 0.68 was reported. Accordingly, further work would be desirable to establish a rigorous theoretical justification for adopting $C_d = 0.615$ in leak rate calculations.

To illustrate the potential use of this digital twin platform, we extend the validated room-temperature predictions of biaxial matrix-crack density and helium leakage (see Figs. 10-11) to hydrogen leakage at

$-253°C$, explicitly accounting for multiscale thermal residual stresses and incorporating degraded matrix and interface fracture properties. Although systematic equi-biaxial datasets at $-253°C$ are not yet available for direct validation [49], the framework enables constituent-informed sensitivity studies that quantify how cryogenic matrix toughness governs gas-percolation onset and leakage-threshold strain: doubling the cryogenic matrix toughness increases the gas-percolation threshold from $\varepsilon_{cp} = 0.33\%$ to $\varepsilon_{cp} = 0.48\%$ (see Fig. 12), indicating the scope for significantly improving CFRPs' anti-leakage performance at cryogenic temperatures through matrix toughening. Notably, our previous nano-toughening studies [44-47, 51] have demonstrated that cryogenic epoxy fracture energy can be increased several-fold relative to an unmodified matrix, suggesting a practical route to extend the allowable operating window (i.e. leakage-threshold pressure) of Type-V CFRP LH_2 vessels. Furthermore, the present multiscale framework provides a pathway to future integration with molecular-dynamics-informed constituent and interface properties [52], moving toward increasingly first-principles predictions of structural integrity and gas leak rates for cryogenic pressure vessels.

7 Conclusion

This study develops a multiscale modelling framework to predict the percolation of matrix cracks and gas leak rate of carbon fibre reinforced composites under thermomechanical loading, including biaxial tension at cryogenic temperatures where the direct measurements are often very challenging. The key contributions include a scale bridging strategy and a digital twin model that uses constituent properties to determine key damage-state variables required by multilayer conductance leakage calculations. Specifically, we have demonstrated a new framework for determining (a) the ply-wise matrix crack density and (b) the crack-intersection opening and associated throat area that governs local conductance. By eliminating post-mortem or destructive experimental testing to quantify crack density and empirical calibration of an effective conductance used in prior analyses, the proposed framework provides a method to fully characterize damage-to-leakage chain, enabling direct prediction of the leak-rate–load response and the leakage-threshold load for CFRP laminates at both room and cryogenic temperatures.

The matrix crack density evolution is predicted using a multiscale MDM–CDM approach. A micromechanical RVE derives matrix-dominated strengths, fracture energies, and mixed-mode softening laws that are directly upscaled to a 3D laminate CDM model under combined thermal and mechanical loading. This approach has been shown to reduce reliance on a large set of independently identified ply-level CDM parameters, many of which lack standardized test methods and become increasingly difficult to isolate at cryogenic temperatures where multiple competing damage modes may interact in highly nonlinear ways. The resulting modelling capability is therefore well suited to quantify cryogenic effects, such as thermal residual stresses and

temperature-dependent matrix toughness on matrix cracking onset and progression. Furthermore, because true biaxial coupon testing, particularly at cryogenic temperatures, may not be readily accessible, present simulations indicate that a more practical sequential uniaxial protocol can reproduce key biaxial damage response of cross-ply laminates; experimental validation of this surrogate protocol is proposed in future work.

With the crack-density states predicted by the MDM–CDM at each load level, a computationally efficient and accurate doubly periodic unit-cell model with a prescribed cohesive network is used to resolve local crack-intersection openings and the associated throat areas that govern gas conductance. These matrix cracking descriptors are then coupled to a compressible-gas orifice/multilayer conductance formulation to compute the through-thickness leak-rate response under combined thermal and mechanical loading. Excellent agreement with published helium leak-rate measurements obtained after biaxial loading at multiple biaxiality ratios demonstrates the predictive capability of the framework. The validated model is subsequently applied to predict *in-situ* hydrogen leak rate under biaxial loading at both room temperature and $-253°C$, for which corresponding experimental data are not currently available. Leakage-threshold strains are identified by benchmarking against allowable limits in current qualification standards, and the cryogenic predictions further quantify the benefit of matrix toughening in increasing the threshold. Overall, the present modelling framework offers a physics-based digital twin capability for CFRP composites, enabling earlier screening of material design options and reducing iteration prior to full-scale vessel proof tests, while informing future analysis-supported leakage criteria for CFRP vessel standards.

Declaration of competing interest

The authors declare that they have no known competing financial interests or personal relationships that could have appeared to influence the work reported in this paper.

Acknowledgements

The authors are thankful for the financial support received from US Air Force Research Laboratory's Asian Office of Aerospace Research and Development Grant (FA2386-25-1-4004) and Australian Research Council's Discovery Grant Program (DP230101204). The authors acknowledge and thank Dr David Mollenhauer and Dr David Newell at AFRL for their insightful and constructive comments, which have significantly contributed to the improvement of this work.

References

[1] I. Katsivalis, V. Signorini, F. Ohlsson, C. Langhammer, M. Minelli, L.E. Asp, Hydrogen permeability of thin-ply composites after mechanical loading, Compos. - A: Appl. Sci. Manuf. 176 (2024) 107867.

[2] N. Fleck, Compressive failure of fiber composites, Adv. Appl. Mech. 33 (1997) 43-117.

[3] J. Hohe, A. Neubrand, S. Fliegener, C. Beckmann, M. Schober, K.-P. Weiss, S. Appel, Performance of fiber reinforced materials under cryogenic conditions—A review, Compos. - A: Appl. Sci. Manuf. 141 (2021) 106226.

[4] J.-M. Berthelot, Transverse cracking and delamination in cross-ply glass-fiber and carbon-fiber reinforced plastic laminates: Static and fatigue loading, Appl. Mech. Rev. 56(1) (2003) 111-147.

[5] J. Llobet, P. Maimí, Y. Essa, F.M. de la Escalera, Progressive matrix cracking in carbon/epoxy cross-ply laminates under static and fatigue loading, Int. J. Fatigue 119 (2019) 330-337.

[6] P. Maimi, P. Camanho, J. Mayugo, A. Turon, Matrix cracking and delamination in laminated composites. Part II: Evolution of crack density and delamination, Mech. Mater. 43 (2011) 194-211.

[7] H. Kumazawa, T. Aoki, I. Susuki, Analysis and experiment of gas leakage through composite laminates for propellant tanks, AIAA. J. 41 (2003) 2037-2044.

[8] T. Yokozeki, T. Ogasawara, T. Aoki, T. Ishikawa, Experimental evaluation of gas permeability through damaged composite laminates for cryogenic tank, Compos. Sci. Technol. 69 (2009) 1334-1340.

[9] J. Bae, J. Jin, J. Yun, S. Park, J. Lee, Nano-engineered permeation barriers for composite laminates: Polyamide nanofiber interlayers for cryogenic cycling durability and gas-barrier performance, Compos. B Eng. (2025) 113219.

[10] ISO 11119-3 Gas cylinders—Design, construction and testing of refillable composite gas cylinders and tubes, International Organization for Standardization, Switzerland, 2020.

[11] ISO 15869 Gaseous hydrogen and hydrogen blends — Land vehicle fuel tanks, International Organization for Standardization, London, 2009.

[12] ISO 19881 Gaseous hydrogen - Land vehicle fuel containers, International Organization for Standardization, Switzerland, 2025.

[13] UN GTR No.13 Global technical regulation on hydrogen and fuel cell vehicles, United Nations, 2013.

[14] SAE J2579 Standard for Fuel Systems in Fuel Cell and Other Hydrogen Vehicles, SAE International Technical Standard, 2023.

[15] ANSI/AIAA S-081B-2018 Space Systems—Composite Overwrapped Pressure Vessels, American National Standard, USA, 2018.

[16] EN 12245 Transportable gas cylinders-Fully wrapped composite cylinders, European Standard, 2022.

[17] M.J. Robinson, Determination of allowable hydrogen permeation rates for launch vehicle propellant tanks, J. Spacecr. Rockets. 45 (2008) 82-89.

[18] H. Kumazawa, I. Susuki, T. Aoki, Gas leakage evaluation of CFRP cross-ply laminates under biaxial loadings, J. Compos. Mater. 40 (2006) 853-871.

[19] H. Kumazawa, H. Hayashi, I. Susuki, T. Utsunomiya, Damage and permeability evolution in CFRP cross-ply laminates, Compos. Struct. 76 (2006) 73-81.

[20] S. Roy, M. Benjamin, Modeling of permeation and damage in graphite/epoxy laminates for cryogenic fuel storage, Compos. Sci. Technol. 64 (2004) 2051-2065.

[21] H. Hamori, H. Kumazawa, R. Higuchi, T. Yokozeki, Gas permeability of CFRP cross-ply laminates with thin-ply barrier layers under cryogenic and biaxial loading conditions, Compos. Struct. 245 (2020) 112326.

[22] H. Kumazawa, J. Whitcomb, Numerical modeling of gas leakage through damaged composite laminates, J. Compos. Mater. 42 (2008) 1619-1638.

[23] M. Elices, G. Guinea, J. Gomez, J. Planas, The cohesive zone model: advantages, limitations and challenges, Eng. Fract. Mech. 69 (2002) 137-163.

[24] M. Joosten, Q. Yang, M. Blacklock, C. Wang, A cohesive network approach for modelling fibre and matrix damage in composite laminates, Compos. Struct. 206 (2018) 658-667.

[25] W. Chang, L.F. Rose, B. Jiang, A.J. Kinloch, C.H. Wang, Can micromechanical modelling determine the continuum damage model inputs for matrix-dominated failure in fibre-reinforced polymer composites?, Compos. B Eng. 308 (2026) 112978.

[26] P. Maimí, P.P. Camanho, J. Mayugo, C. Dávila, A continuum damage model for composite laminates: Part II–Computational implementation and validation, Mech. Mater. 39 (2007) 909-919.

[27] H. Liu, J. Liu, Y. Ding, Z.E. Hall, X. Kong, J. Zhou, B.R. Blackman, A.J. Kinloch, J.P. Dear, A three-dimensional elastic-plastic damage model for predicting the impact behaviour of fibre-reinforced polymer-matrix composites, Compos. B Eng. 201 (2020) 108389.

[28] P. Shabani, L. Li, J. Laliberte, G. Qi, D. Rapking, D. Mollenhauer, High-fidelity simulation of low-velocity impact damage in fiber-reinforced composite laminates using integrated discrete and continuum damage models, Compos. Struct. 313 (2023) 116910.

[29] Z.P. Bažant, B.H. Oh, Crack band theory for fracture of concrete, Mater. Constr. 16 (1983) 155-177.

[30] A. Arteiro, G. Catalanotti, J. Reinoso, P. Linde, P.P. Camanho, Simulation of the mechanical response of thin-ply composites: from computational micro-mechanics to structural analysis, Arch. Comput. Methods. Eng. 26 (2019) 1445-1487.

[31] C.H. Kurita, Critical Flow Restricting Orifices, U.S. Department of Energy Office of Scientific and Technical Information, United States, 1988.

[32] X. Tu, P. Hrnjak, C. Bullard, Flow of R134a Through Micro-Orifices, International Refrigeration and Air Conditioning Conference, Purdue University, 2002.

[33] T. Hasegawa, M. Suganuma, H. Watanabe, Anomaly of excess pressure drops of the flow through very small orifices, Phys. Fluids 9 (1997) 1-3.

[34] W. Chang, L.R.F. Rose, S. Wu, A.J. Kinloch, C.H. Wang, Increasing crack growth resistance for through-thickness matrix cracking and its role in suppressing ply cracking in thin-ply laminates, Compos. - A: Appl. Sci. Manuf. 163 (2022) 107219.

[35] ABAQUS 2024 Documentation, Dassault Systèmes Simulia Corp., Providence, 2024.

[36] Q. Sun, Z. Meng, G. Zhou, S.-P. Lin, H. Kang, S. Keten, H. Guo, X. Su, Multi-scale computational analysis of unidirectional carbon fiber reinforced polymer composites under various loading conditions, Compos. Struct. 196 (2018) 30-43.

[37] P.P. Camanho, C.G. Davila, M. De Moura, Numerical simulation of mixed-mode progressive delamination in composite materials, J. Compos. Mater. 37 (2003) 1415-1438.

[38] ISO 5167-1:2003 Measurement of fluid flow by means of pressure differential devices inserted in circular cross-section conduits running full - Part 1: General principles and requirements., International Organization for Standardization, 2003.

[39] R.W. Miller, Flow measurement engineering handbook, U.S. Department of Energy, New York: McGraw-Hill., 1996.

[40] H.S. Bean, Fluid Meters (6th ed.), The American Society of Mechanical Engineers (ASME), 1983.

[41] T.L. Anderson, Fracture mechanics: fundamentals and applications (fourth ed.), CRC Press, USA, 2017.

[42] T.W. Clyne, D. Hull, An introduction to composite materials, Cambridge university press, 2019.

[43] A. Turon, C.G. Davila, P.P. Camanho, J. Costa, An engineering solution for mesh size effects in the simulation of delamination using cohesive zone models, Eng. Fract. Mech. 74(10) (2007) 1665-1682.

[44] J. Wang, W. Chang, M.S. Islam, F. Huang, S. Wu, L.F. Rose, J. Zhang, C.H. Wang, Toughening epoxy by nano-structured block copolymer to mitigate matrix microcracking of carbon fibre composites at cryogenic temperatures, Compos. Sci. Technol. 251 (2024) 110548.

[45] W. Chang, L.R.F. Rose, M.S. Islam, S. Wu, S. Peng, F. Huang, A.J. Kinloch, C.H. Wang, Strengthening and toughening epoxy polymer at cryogenic temperature using cupric oxide nanorods, Compos. Sci. Technol. 208 (2021) 108762.

[46] B. Jiang, W. Chang, X. Wang, Z. Sha, G. Pearce, L.F. Rose, A.J. Kinloch, C.H. Wang, Increasing the flame retardancy and cryogenic toughness of an epoxy polymer using polydopamine nanoparticles, Compos. B Eng. 304 (2025) 112675.

[47] W. Chang, L.F. Rose, Z. Sha, F. Huang, A.J. Kinloch, C.H. Wang, Multiscale modelling of nanoparticle toughening in epoxy: Effects of particle-matrix interface, particle size, and volume fraction, Compos. Sci. Technol. 256 (2024) 110788.

[48] W. Chang, F. Rose, S. Wu, A. Kinloch, C. Wang, Through-thickness crack growth resistance in fibre composites and its role in preventing ply cracking in cross-ply laminates, Eng. rXiv. (2022).

[49] M. Bodaghi, H.Y. Nezhad, M. Nikzad, C.G. Bayreuther, P. Nowakoski, M. Koerdt, C. Polle, A. Krenz, B. Maack, D. May, A review of technical challenges and research gaps to address permeability controls in cryogenic composite hydrogen tanks, Compos. B Eng. 315 (2026) 113427.

[50] P. Peddiraju, J. Noh, J. Whitcomb, D.C. Lagoudas, Prediction of cryogen leak rate through damaged composite laminates, J. Compos. Mater. 41 (2007) 41-71.

[51] M.S. Islam, W. Chang, Z. Sha, J. Wang, S. Wu, L.F. Rose, A.J. Kinloch, C.H. Wang, Mitigating cryogenic microcracking in carbon-fibre reinforced polymer composites using negative thermal-expansion nanoparticles functionalized by a polydopamine coating, Compos. B Eng. 257 (2023) 110676.

[52] S.C. Chowdhury, J.W. Gillespie Jr, Strain-rate dependent mixed-mode traction laws for glass fiber-epoxy interphase using molecular dynamics simulations, Compos. B Eng. 275 (2024) 111351.